Microstructured antireflective encapsulant on concentrator solar cells

Gavin P Forcade, Arnaud Ritou, Philippe St-pierre, Olivier Dellea, Maïté Volatier, Abdelatif Jaouad, Christopher E Valdivia, Karin Hinzer, Maxime Darnon

Received: 10 May 2021 | Revised: 22 July 2021 | Accepted: 20 August 2021

DOI: 10.1002/pip.3468

RESEARCH ARTICLE

PROGRESS IN PHOTOVOLTAICS WILEY

Microstructured antireflective encapsulant on concentrator solar cells

Gavin P. Forcade[1] | Arnaud Ritou[2,3] | Philippe St-Pierre[2,3] | Olivier Dellea[4] | Maïté Volatier[2,3] | Abdelatif Jaouad[2,3] | Christopher E. Valdivia[1] | Karin Hinzer[1] | Maxime Darnon[2,3]

[1]SUNLAB Centre for Research in Photonics, University of Ottawa, Ottawa, Ontario, Canada

[2]Laboratoire Nanotechnologies Nanosystèmes (LN2), CNRS, Université de Sherbrooke, Sherbrooke, Québec, Canada

[3]Institut Interdisciplinaire d'Innovation Technologique (3IT), Université de Sherbrooke, Sherbrooke, Québec, Canada

[4]CEA, Liten, DTNM, Université Grenoble Alpes, Grenoble, France

Correspondence
Maxime Darnon, Institut Interdisciplinaire d'Innovation Technologique (3IT), 3000 Boulevard de l'Université, Sherbrooke, Qc, J1K015, Canada.
Email: maxime.darnon@usherbrooke.ca

Funding information
Fonds de Recherche du Québec Nature et Technologie; Quebec Ministère de l'Économie, de la Science et de l'Innovation; MITACS; STACE

Abstract

Microstructured antireflective coatings (ARCs) can reduce reflection losses over a wide range of incidence angles when applied to the surface of a high-efficiency III-V photovoltaic cell in a concentrator photovoltaic (CPV) system. In this article, we present a microstructured ARC consisting of a monolayer of close-packed silica microbeads partially submerged within a polydimethylsiloxane (PDMS) cell encapsulant for use within a reference 500× CPV submodule. Comparing a commercialized SiO_x encapsulant to this microstructured coating with 25% submerged 1,000 nm-diameter beads, angle-dependent external quantum efficiency measurements yield a 2.6% current gain for the microstructured coating. Simulations demonstrate good agreement with measurements, predicting a 2.4% current gain for the same configuration. Extrapolating with our validated model, we estimate a maximum and achievable (within a large manufacturing tolerance) current gain of 3.4% and 2.9 ± 0.4% using 60% submerged and 10%–32% submerged 760 nm-diameter beads, respectively.

KEYWORDS
antireflection, concentrator photovoltaic, encapsulant, external quantum efficiency, microstructuring, ray tracing, RCWA, TMM

1 | INTRODUCTION

Concentrator photovoltaic (CPV) systems can be less costly than Si PV in high DNI regions[1,2] with lower lifecycle impacts and a smaller energy payback time.[3,4] Sustained technological advances have significantly reduced CPV costs by increasing system efficiency.[5] Among the largest losses, optical reflections are generally minimized by depositing an antireflective coating (ARC) on the surface of the photovoltaic cell. Most CPV systems use high-efficiency triple-junction solar cells (3JSCs) with a multilayer ARC made from two or more thin transparent layers of increasing refractive index. Patterned surfaces, or moth-eye structures, offer the potential for improved performance in comparison with standard ARC designs, reducing reflections over a wide range of incidence angles. Either nanometric or micrometric structures create an effective refractive index gradient that smooths the optical transition between two media.[6] Such ARC structures can be effective over a wide spectral range and insensitive to the polarization of incident light.[7]

Several methods have been studied to achieve surface microstructuring, either depositing or removing material to create

the structures. Deposition approaches include sol–gel processing,[8,9] glancing angle deposition,[10–15] and colloidal infiltration with etching.[16] Conversely, material removal approaches include colloidal nanosphere lithography[17–20] or laser interference lithography[21] combined with an etching step. Of these, only some sol–gel methods are performed under atmospheric pressure and do not require microfabrication techniques. García-Linares et al. demonstrated the concept of an ARC consisting of a layer of silica microbeads[22] deposited by a colloidal sol–gel method.[23] That study showed a 1.8% increase in short-circuit current density (J_{sc}) for normally incident irradiance on a 3JSC with 530 nm beads deposited on a silicone encapsulant, as compared with the same cell without beads. Their study included a simulation suggesting that beads submerged halfway into the silicone could potentially provide greater gains. Simulations carried out by Forcade et al.[24] showed that controlling the submergence of the beads in a layer of silicone can also improve the temperature dependency of a concentrator system and led to a J_{sc} enhancement up to 2.6%, compared with devices without beads.

The objective of this work is to study and understand the performance enhancements of a microstructure produced from an ordered monolayer of silica beads deposited on a polydimethylsiloxane (PDMS) encapsulant layer for a 3JSC. The novelty of our work lies in the improved deposition process allowing greater control over the microbead submergence into PDMS. We measure and compare the 3JSC J_{sc} gain for various ARCs and use the results to calibrate our model. We then employ our calibrated model to optimize the bead size and submergence into PDMS to maximize the electrical performance of the 3JSC.

In this work, we study a 500× CPV system composed of a $50 \times 50\ mm^2$ silicone-on-glass (SoG) Fresnel lens concentrating direct sunlight onto a hexagonally shaped high-efficiency 3JSC at its focal length (93 mm), as depicted in Figure 1A. Each hexagonal cell is 3 mm in width and has a grid line pattern optimized for a 500× concentration ratio (Figure 1B). Finally, the cells are coated with a dual-layer thin film ARC of AlO_x/TiO_x optimized for an encapsulating layer with refractive index near 1.5 (Figure 1C). Presently, STACE 500× modules have a 100 ± 30 nm SiO_x encapsulating layer on the 3JSC for an intended use without a secondary optical element (SOE), as shown in Figure 1D. Although the enclosed modules shield the PV devices from most weathering processes, the encapsulation layer is required to protect the 3JSC against moisture and oxidation and is deposited with an atmospheric plasma.

Our encapsulation involves coating cells with 6.0 ± 0.2 μm of Sylgard 184 PDMS (Figure 1E),[25] with a refractive index of $n_{PDMS}(650\,nm) = 1.410$.[26] PDMS is a common protective layer for CPV solar cells[27] but induces parasitic reflections at the air/PDMS interface.[28] We minimize this reflection by incorporating a microstructured ARC consisting of a monolayer of silica beads, with refractive index $n_{bead}(650\,nm) = 1.457$,[29] partially submerged into the PDMS layer, as shown in Figure 1F. We calculated the optical properties of the microstructured ARC for 0 to 1,200 nm-diameter beads using our numerical model, which was validated from measurements of 1,000 nm-diameter bead samples.

We compare the current generated by four PV device configurations, shown in Figure 1C–F, while under illumination from the AM1.5D spectrum. Each configuration employs the same commercial 3JSC using an AlO_x/TiO_x ARC with fixed thicknesses, which we take as the reference design for electrical performance. The SiO_x-encapsulated 3JSC is the commercial device design used by STACE. We explore a design consisting of the 3JSC with a PDMS encapsulant and monolayer of silica beads with partial submergence into the PDMS. We do not include results for beads directly on the 3JSC or SiO_x/3JSC (i.e., without PDMS) because the beads do not properly adhere to the AlO_x and SiO_x surfaces. Moreover, our numerical model predicted a decrease in current for the 3JSC with beads but without PDMS, in agreement with previous results.[22] Further discussion is provided in the morphology study section. Finally, we compare all configurations to the 3JSC without SiO_x or PDMS (Figure 1C), which we refer to as our *reference* configuration.

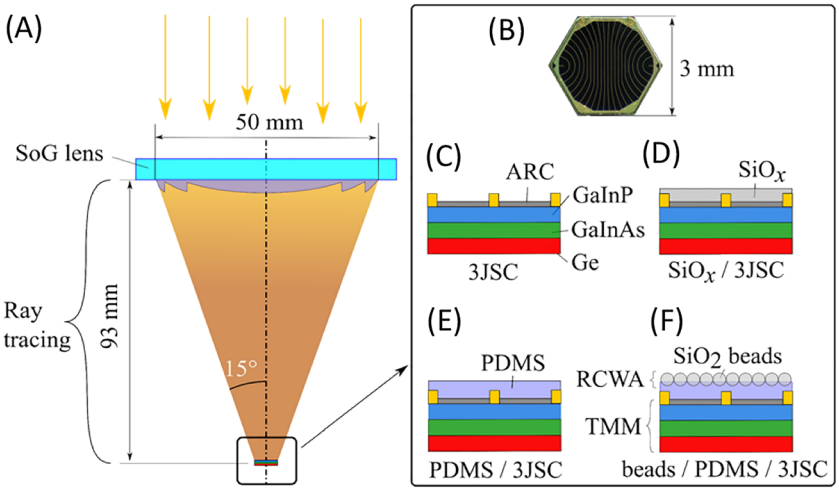

FIGURE 1 (A) Schematic cross section of the concentrator photovoltaic (CPV) submodule. (B) Top view of cell, and cross sections (not to scale) of (C) bare triple-junction solar cell (3JSC), (D) STACE SiO_x encapsulated 3JSC, (E) polydimethylsiloxane (PDMS)-coated 3JSC, and (F) patterned microbead layer partially submerged into a PDMS layer encapsulating the 3JSC [Colour figure can be viewed at wileyonlinelibrary.com]

2 | EXPERIMENTAL STUDY

2.1 | Fabrication

To deposit the PDMS layer, we spin coat liquid PDMS on a 3JSC at a spin rate of 6,000 rpm for 120 s to obtain a thickness of 6.0 ± 0.2 μm. Simulations confirm that the PDMS layer is optically incoherent and that the thickness uncertainty has negligible effects on the optical performance of the device. Subsequently, we deposit a monolayer of hexagonally close-packed silica beads on the PDMS, using a patented method based on a dynamic fluid flow process, called Boostream, described in Delléa and Lebaigue.[30] This method involves first depositing the beads on an easy-to-handle substrate,[31] then transferring them onto the PDMS surface.

As illustrated in Figure 2, the beads can be controllably submerged into the PDMS layer via a curing step. We define the *submergence* of the beads into the PDMS as the depth the beads penetrate below the PDMS surface, normalized to the bead diameter. Prior to the deposition of the beads, the PDMS is partially heat-cured for a time t_1, referred to as the pre-cure. Once the beads are deposited, they are left to rest and sink in the PDMS for a time t_{rest} at room temperature. A final bake referred to as the post-cure, lasting $t_2 = 20\ \text{min} - t_1$, is performed to complete the crosslinking of the PDMS, complying with $t_1 + t_2$ fixed at 20 min at 125°C as instructed in the Sylgard 184 guidebook.[25] The pre-cure fraction, $t_1/(t_1 + t_2)$, represents the percentage of PDMS cure-time completed before bead deposition and is proportional to the chemical crosslinking that converts liquid PDMS to a solid.[32] The submergence of the beads is assessed by analyzing 4–10 beads per sample with cross-sectional scanning electron microscopy (SEM) images as in the example in Figure 2C. The analyzed beads are either at various locations on a sample or on one SEM image.

Figure 3 shows the submergence of 500 and 1,000 nm beads in PDMS as a function of its pre-cure fraction. The four curves correspond to various resting times (t_{rest}) and bead diameters. The colored regions delimit the minimum and maximum measured submergences for several beads on the same sample. For a pre-cure fraction <15%, 500 nm beads were completely submerged into PDMS. The 15% threshold is representative of the gel point, that is, the transition point between liquid and solid PDMS. For a pre-cure fraction >15%, the average bead submergence comprises between 10% and 32%, with a lower submergence for larger pre-cure fractions. For pre-cure fractions between 30% and 50%, 1,000 nm-diameter beads tend to have a larger submergence than 500 nm-diameter beads. For t_{rest} between 1 and 21 h, a similar submergence is observed indicating that within these process conditions, the rest time has little impact on the bead's submergence.

Results from our numerical model, described in Section 3, show a significant improvement for the beads/PDMS/3JSC over the 3JSC configuration with little sensitivity to the submergence. For instance, in Figure 8B, we calculate a current gain of 3%–4% for 1,000 nm-diameter beads submerged 10%–70%. The experimental results of Figure 3 indicate that the process window to obtain a submergence in this range is very broad and corresponds to a pre-cure fraction larger than 15% and rest time between 1 and 21 h. To

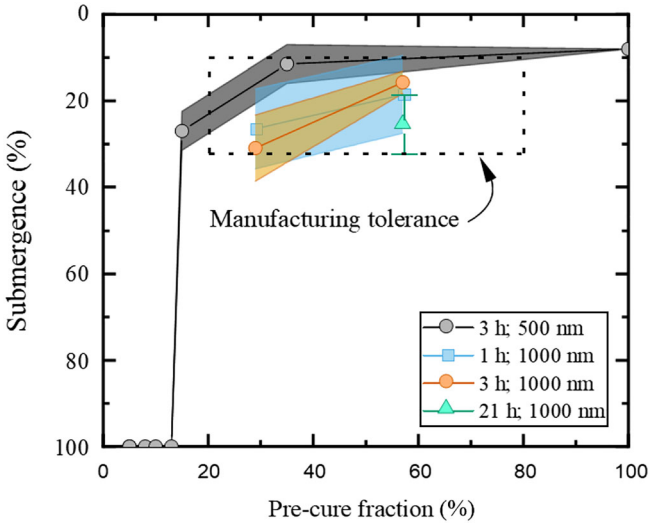

FIGURE 3 Submergence of 500- and 1,000-nm beads in polydimethylsiloxane (PDMS) as a function of the pre-cure fraction of PDMS corresponding to three resting times [Colour figure can be viewed at wileyonlinelibrary.com]

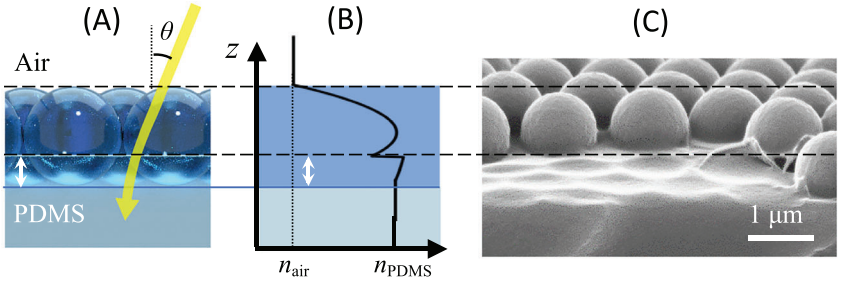

FIGURE 2 (A) Cross-sectional depiction of a microstructured layer made from ordered close-packed silica beads partially submerged into polydimethylsiloxane (PDMS). (B) Representation of the effective refractive index as function of depth across the structured interface, from air (n_{air}) to PDMS (n_{PDMS}). (C) Angled scanning electron microscope view of 1,000 nm-diameter beads submerged ~25% into the PDMS layer [Colour figure can be viewed at wileyonlinelibrary.com]

highlight the high manufacturing tolerance of the beads/PDMS encapsulant, we define a wide processing range of 20%–80% pre-cure fraction that corresponds to 10%–32% submergence and is represented by the dotted rectangle in Figure 3. These boundaries will be used to calculate the achievable performance of the beads/PDMS/3JSC configuration.

2.2 | Morphology study

Microbead layers were inspected for uniformity, defect density, and submergence into PDMS. Figure 4A shows an optical microscopy image of beads deposited on SiO_x/3JSC, whereas Figure 4B–D show SEM images of beads deposited on PDMS/3JSC, typically forming a uniform partially submerged 2D hexagonal close-packed monolayer structure throughout the surface. Beads exhibit better adherence to PDMS than to SiO_x due to their submergence into the soft PDMS layer (Figure 4D) and due to the strong hydrogen bonds between silica beads and terminating silanol groups of PDMS. The 6 μm-thick PDMS layer smooths out the topography of the cell surface by covering the ~2 μm-thick metal fingers, visible as the dark band in Figure 4C. Figure 4B is representative of the flat monolayer formed by the beads with only a few topology defects. Only 10 vacancies are counted in the $130 \times 90\ \mu m^2$ area ($<10^4/cm^2$), but more cracks with various widths and lengths are visible. From the 9,900 beads counted in this image, 8,750 have six nearest neighbors; meaning, 88% of the structure is hexagonally close packed. However, studying similar structures to ours (i.e. domes patterned pseudo-periodically across a flat surface), Battaglia et al.[33] and Ferry et al.[34] demonstrated an equivalent J_{sc} using either random or periodic structures.

From our SEM investigations, we did not observe any defects in the PDMS layers such as cracks, bubbling, or swelling.

2.3 | Characterization method

The microstructure formed by the bead monolayer increases the light intensity entering the cell, influencing the electric current. To quantify this performance enhancement, we calculate the cell's J_{sc} by integrating the external quantum efficiency (EQE) with the 1-sun AM1.5D spectrum (900 W/m^2), taking the smallest J_{sc} of the three series-connected junctions. The J_{sc} gain is then defined as the relative difference between sample configurations shown in Figure 1D–F and the reference device (Figure 1C):

$$\Delta J_{sc} = \frac{\left[J_{sc}^{i} - J_{sc}^{Ref}\right]}{J_{sc}^{Ref}}, \quad (1)$$

where *i* denotes the device configuration to be compared with the reference device, *Ref*. The EQE (Figure 5) is measured on a PV measurement QEX7 system at 3IT, with filtered white light, and voltage biasing to ensure the subcell of interest is in short circuit. The EQE measurement procedure follows the methodology proposed by Meusel et al.[35] We maintained the samples at 25°C during measurements. We also measured the angular dependent EQE, by placing our samples on tapered holders for incident angles up to 30°.

Our numerical model required the internal quantum efficiency (IQE) of the 3JSC as a main input. Therefore, we measured the IQE (Figure 5) using an Oriel IQE-200 test station following the same procedure as the EQE measurements above, while simultaneously measuring specular reflection. However, points at 825, 885, and 965–1,020 nm were manually smoothed by interpolating between adjacent points, due to high variability at the xenon lamp spectrum peaks. The smoothing performed at 965–1020 nm mainly affects the bottom subcell, which overproduces current for all our configurations, and therefore does not affect the outcome of our results. The bottom

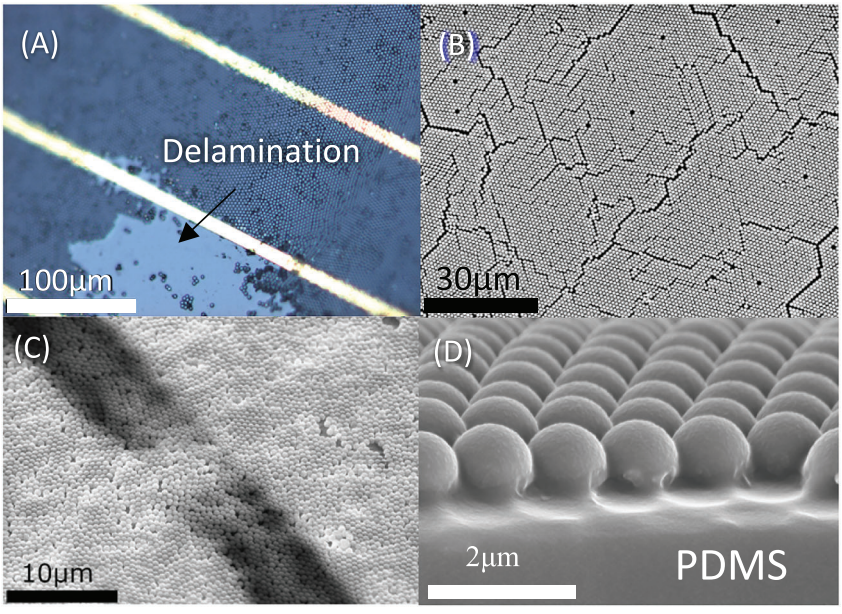

FIGURE 4 Micrographs of beads deposited on: (A) SiO_x and (B–D) polydimethylsiloxane (PDMS). (A) Delamination of the beads (optical microscope); (B) top view image (scanning electron microscopy [SEM]); (C) 45° view of a metal finger (dark band) underneath the beads/PDMS coating (SEM); and (D) glancing angle cross-sectional close-up (SEM) [Colour figure can be viewed at wileyonlinelibrary.com]

subcell QE artifact is corrected using the method described in Ferry et al.[36] Comparing the EQE to the IQE and reflection in Figure 5 confirms that the QE measured by both QEX7 and Oriel IQE-200 systems is in good agreement.

2.4 | Measured current gain

Solar cells were fabricated in the four configurations shown in Figure 1C–F, to compare their electrical properties. We investigate the commercial design consisting of a 3JSC with an atmospheric plasma deposited SiO_x layer acting as both a third layer to the ARC and an encapsulant. We explore the benefits of the PDMS encapsulant as well as the microstructured surface composed of 1,000 nm-diameter beads submerged ~25% into PDMS.

Figure 6 shows the J_{sc} gain (calculated using Equation 1) for normally incident light on the four types of configurations. The gain is averaged over the number of devices measured, which is represented by the number in parenthesis, with an error bar width equal to the difference between the maximum and minimum J_{sc} gain of all samples. The SiO_x encapsulating layer improves the J_{sc} by 1.1 ± 1.6% over the reference 3JSC. This increase is expected because the dual-layer ARC is optimized for the refractive index of silica. The J_{sc} gain of SiO_x/3JSC has a large uncertainty because the encapsulating layer is deposited by an atmospheric plasma, which fabricates thin films with relatively large variations in thickness and refractive index but at fast speeds and low costs.[37] With a similar refractive index, PDMS improves the J_{sc} by 1.8 ± 0.6% from the reference. The uncertainty is smaller because light travels incoherently within the optically thick PDMS layer, which makes thickness and refractive index variations unimportant. Finally, adding a monolayer of 1,000 nm-diameter beads on PDMS improves the J_{sc} up to 3.7 ± 1% from the reference, which is the largest gain demonstrated here. The slightly higher uncertainty for beads/PDMS/3JSC is attributed to sample-to-sample variation of bead submergence.

Figure 7 investigates the measured angle-dependent current produced by the reference 3JSC, the commercial SiO_x/3JSC, and beads/PDMS/3JSC with 1,000 nm-diameter beads submerged 25% into the PDMS encapsulant. The histogram in Figure 7A displays the calculated angular distribution of irradiance on the cell in the simulated submodule represented in Figure 1A and previously shown in Forcade et al.[24] Notice that most of the irradiance comes within an incident angle of 10–15°, as is expected for these square lenses. Figure 7B shows an increasing J_{sc} with angle for both encapsulated cells but the opposite for the reference device. This amplifies the J_{sc} gain calculated in Figure 7C, reaching 5% at 30°. The error bar range is calculated by taking the difference between the maximum and

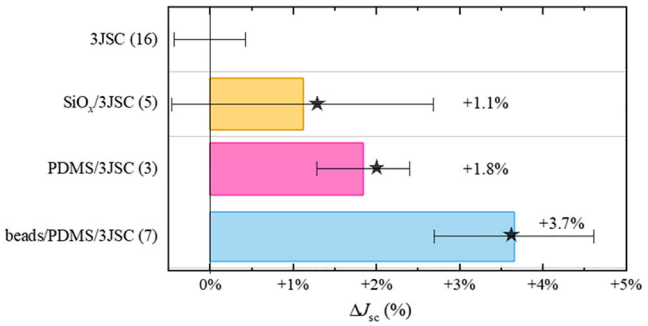

FIGURE 6 Current density gain between each device configuration and the reference, averaged over the number of tested photovoltaic (PV) devices shown in parenthesis, operating at 25°C. Black stars are the values calculated by our numerical model [Colour figure can be viewed at wileyonlinelibrary.com]

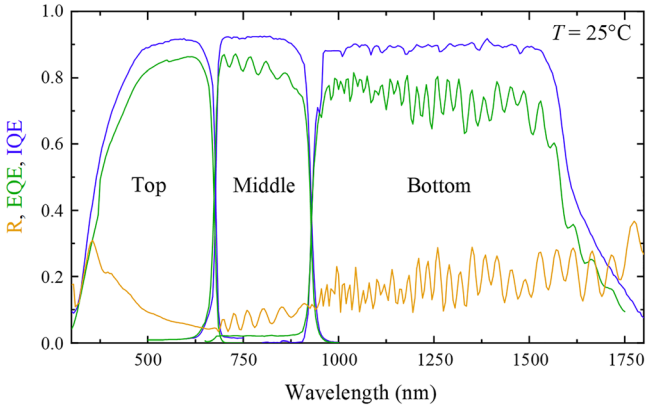

FIGURE 5 The measured internal and external quantum efficiency (IQE and EQE) of the top, middle, and bottom junction of the reference triple-junction solar cell (3JSC), together with the specular reflectance (R) [Colour figure can be viewed at wileyonlinelibrary.com]

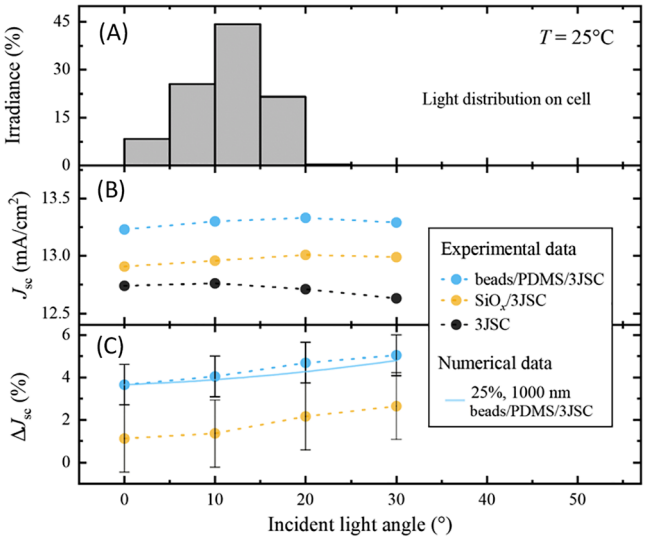

FIGURE 7 (A) Calculated angular distribution of irradiance on the cell in the 500× concentrator photovoltaic (CPV) submodule. (B) Measured J_{sc} as a function of the angle of incidence. (C) J_{sc} gain between the encapsulated and reference devices [Colour figure can be viewed at wileyonlinelibrary.com]

minimum J_{sc} gain for normally incident light, and we assume the uncertainty is constant for all angles measured. The solid blue line presents the simulated gain for the beads/PDMS/3JSC configuration for 25% bead submergence, showing good agreement with measurement.

3 | SIMULATION STUDY

3.1 | Numerical model

We have developed a computational model to simulate the optical properties of the CPV submodule, combining ray tracing, rigorous coupled wave analysis (RCWA), and the transfer matrix method (TMM) within different regions of the submodule, as shown in Figure 1. These calculations provide the fraction of rays transmitted into the 3JSC at a wavelength interval of 300–1,800 nm, which we weight by the AM1.5D solar spectrum and the measured IQE (Figure 5) to calculate the J_{sc} of the cell. Calculations of these wavelength-dependent transmissions across the beads/PMDS interface are presented in Forcade et al.[24] for several bead sizes.

The commercial ray tracing software, Zemax OpticStudio, sends incoherent rays through the Fresnel lens to the solar cell. Because ray tracing is unable to resolve scattering for the sub- and/or near-wavelength structure formed at the beads/PDMS interface, we employed an open-source RCWA code, RETICOLO,[38] to compute a bidirectional scattering distribution function (BSDF). The BSDF was then applied as an interface within OpticStudio to account for light transmitting from air into the PDMS layer and for light trapping within the PDMS layer. Rays transmitted into the PDMS layer travel incoherently, reaching the PDMS/3JSC interface, where they transmit and reflect via a boundary condition set by TMM[39] calculations of the 3JSC layer structure detailed in Figure 1C.

To approximate the proprietary design of the commercial 3JSC, we took SEM side-view images of a sliced 3JSC to obtain top layer thicknesses and subsequently fit TMM calculations to reflection measurements of 3JSC and PDMS/3JSC configurations. We achieved the best fit using the complex refractive indexes from Gupta et al., Kim et al., Ochoa-Martínez et al., Cui et al., Djurišić et al., Palik, and Aspnes and Studna.[40–46]

Although we measured a lower J_{sc} for SiO_x/3JSC versus PDMS/3JSC (see Figure 7), we also measured a lower spectral and IQE-weighted reflection for all junctions, which makes our model over-estimate the J_{sc} for the SiO_x/3JSC configuration by almost 5%. To account for the discrepancy, we adopted a SiO_x layer with non-negligible parasitic light absorption, which could be attributed to imperfections arising during deposition. To simulate the SiO_x layer, we applied a similar approach to Bedjaoui et al.[47] and assumed an effective medium with fractions of silica, a–Si, and air. Good match resulted between simulated and measured J_{sc}, while assuring a good fit between reflections, for a layer composed of 19.2% air, 80% silica, 0.8% a–Si, and an added extinction coefficient of $k \sim 0.01$ for all wavelengths in accordance with ellipsometry measurements. The constant extinction coefficient also agrees with absorption measurements of a similar SiO_x layer fabricated by Carneiro et al.[48] We also find that 19.2% porous SiO_x is reasonable because it is a little less than a previously reported porosity for a similar SiO_x layer.[49]

3.2 | Simulated current gain

Figure 8 displays simulated J_{sc} gain (Equation 1) of (A) normally incident and (B) submodule distributed AM1.5D spectrum on the beads/PDMS/3JSC configuration for varying bead diameters and submergence, relative to the reference device. Along the bead diameter axis, simulations used a graded step size starting with large 100 nm steps at the extremities and narrowing to 20 nm steps near the J_{sc}-gain peak, and for the bead submergence axis, we use a constant 10% spacing. The two horizontal-dashed lines represent the range of submergences obtained with 20%–80% precure time, as discussed in Figure 3. Within this window, Figure 8A,B has its highest average J_{sc} gain of 4.8 ± 0.4% and 4.4 ± 0.4% for 760 nm beads, respectively. The maximum J_{sc} gain over all our simulation space for Figure 8A,B is 5.2% and 4.8% for 760 nm beads with 60% submergence, respectively. We also note that our simulations of the beads/PDMS/3JSC configuration were always middle GaInAs subcell limited.

Our RCWA simulations showed that beads of ~760 nm diameter provide an optimal balance between two opposing loss mechanisms.

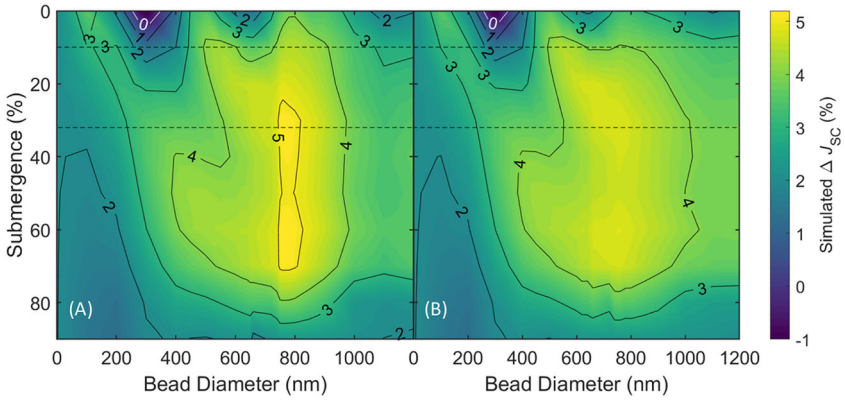

FIGURE 8 Simulated short-circuit current gain for the beads/polydimethylsiloxane (PDMS)/triple-junction solar cell (3JSC) configuration (Figure 1F) relative to the reference device (Figure 1C) as a function of bead size and submergence into PDMS for (A) normally incident light and (B) submodule distributed light. The dashed lines represent the boundaries of the manufacturing tolerance introduced in Figure 3 [Colour figure can be viewed at wileyonlinelibrary.com]

TABLE 1 J_{sc} gain of encapsulated cells (Figure 1D–F) relative to the reference (Figure 1C) for normal and submodule irradiance, comparing measured and simulated results

		Normal irradiance ΔJ_{sc} (%)		Submodule ΔJ_{sc} (%)	
Configuration	**Submergence**	**Meas.**	**Sim.**	**Meas.**	**Sim.**
SiO_x/3JSC	–	1.1 ± 1.6	1.3	1.6 ± 1.6	1.5
1,000-nm beads/PDMS/3JSC	25%	3.7 ± 1.0	3.7	4.2 ± 1.0	3.9
(Maximum)760-nm beads/PDMS/3JSC	60%	–	5.2	–	4.8
(Achievable) 760-nm beads/PDMS/3JSC	10–32%	–	4.8 ± 0.4	–	4.4 ± 0.4

Abbreviations: 3JSC, triple-junction solar cell; PDMS, polydimethylsiloxane.

For smaller beads, the shorter graded refractive index effective medium across the beads/PDMS interface diminishes transmission. For larger beads, stronger optical diffraction increased light scattering and front-surface reflectivity. Beads with a diameter of 760 nm produced diffraction for wavelengths <930 nm, which is near the absorption edge of the current limiting middle subcell (Figure 5). Therefore, both larger and smaller beads diminish the transmission of wavelengths absorbed within the current-limited middle subcell of theses PV devices, making ~760 nm beads the optimal size. Ultimately, the optimal bead size and submergence will depend on the device structure and subcell bandgaps.

Figure 8A,B displays J_{sc} gain oscillating as a function of bead diameter when submerged <50%. The oscillations are due to a reversion of the effective refractive index for the medium between the bead equator and PDMS surface that is dependent on bead diameter and submergence, as depicted in Figure 2B.

4 | DISCUSSION

Table 1 displays J_{sc} gain (Equation 1) for configurations with encapsulation relative to the reference device, comparing measurements to simulations. We show results for both normally incident irradiance and for submodule angular distributed irradiance (Figure 7A), integrated with the angle dependent EQE of devices. As before, the measured uncertainties represent the range between largest and smallest currents measured under normal incidence. The simulated uncertainties encompass all the currents obtained in the process window defined in Figure 3.

We find good agreement between our measurements and simulations for both 1,000 nm beads/PDMS/3JSC and SiO_x/3JSC configurations (see Table 1). Extrapolating with this model, we simulate a maximum gain of 4.8% for 760 nm beads submerged 60% and an achievable gain within the manufacturing tolerance window of 4.4 ± 0.4% for 760 nm beads, relative to the reference device.

Comparing the J_{sc} of simulation-optimized beads/PDMS/3JSC to the commercial SiO_x/3JSC design under normal irradiance (from Table 1), we calculate a maximum increase within our simulation space of 4.0% and an achievable gain within the process window of 3.5 ± 0.4%. Under submodule irradiance, we calculate maximum and achievable current gains of 3.4% and 2.9 ± 0.4%, respectively.

A large J_{sc} uncertainty between PV devices is detrimental to series connected CPV modules, because its current is limited by the worst performing submodule. These losses can be mitigated with bypass diodes but increases manufacturing costs. For the submodule under study (Figure 1A), we measured a large J_{sc} gain variability of 1.6% for the commercial SiO_x/3JSC configuration while only a 1% variability for the 1,000 nm beads/PDMS/3JSC. The J_{sc} gain uncertainty for 760 nm beads/PDMS/3JSC could reach ~1% assuming 0.6% and 0.4% variability from the 3JSC and process window, respectively. Assuming a series-connected CPV module, without bypass diodes and with J_{sc} variability solely from PV devices, we calculate a 3.4% J_{sc} gain for 760 nm beads/PDMS/3JSC relative to the commercial SiO_x/3JSC configuration.

Prior to implementation in commercial CPV systems, the beads/PDMS encapsulant will require further investigation and reliability studies. However, PDMS encapsulants have been extensively studied for CPV systems, showing excellent durability.[27] Partially submerged bead monolayers on PDMS have also demonstrated the ability to withstand harsh processing, such as ultrasonic cleaning.[50] Using an optical microscope, we observed only superficial damages to samples with 1,000 nm beads submerged 25% into PDMS after pick and place manipulation. The beads/PDMS deposition process is compatible with full-wafer manufacturing processes but has yet to be tested. Further study is needed to verify compatibility with all packaging steps, such as for cell singulation, soldering and wire-bonding.

5 | CONCLUSION

We presented a reliable method to produce a microstructured encapsulant coating using PDMS and silica microbeads on CPV solar cells. This method is based on a ~6 μm-thick encapsulating PDMS layer deposited on the 3JSC with a monolayer of hexagonal close-packed silica microbeads partially submerged into it and acts as an integral part of the ARC coating. The results presented here involve the control of the bead submergence into the PDMS layer via curing conditions, which was sufficient to reach a current gain close to the

maximum calculated within the simulation space. This fast-manufacturing process creates reproducible results without the use of expensive microfabrication methods or equipment.

We compared the angle dependent performance of a commercial SiO_x encapsulant to our beads/PDMS encapsulant, for STACE CPV modules using a single 3JSC design. By integrating measured angle-dependent EQE over the angular distribution of light on the cell in the 500× CPV submodule, we measure 1.6 ± 1.6% and 4.2 ± 1% J_{sc} gains for SiO_x/3JSC and beads/PDMS/3JSC with 1,000 nm-diameter beads submerged 25% into PDMS relative to the reference 3JSC, respectively. This was in good agreement with simulations which gave an increase of 1.5% and 3.9%, respectively. Our numerical model, validated by experimental data, predicts a maximum gain of 4.8% for beads/PDM/3JSC with 760 nm-diameter beads submerged 60% into PDMS, over 3JSC devices. In addition, we defined a large manufacturing tolerance window that provides a submergence control of 10%–32% and calculated an achievable gain of 4.4 ± 0.4% for 760 nm beads over 3JSC, where the uncertainty encompasses all values within the process window. For a series-connected CPV module without bypass diodes, we predict an average module current increase of 3.4% for the optimized beads/PDMS/3JSC configuration manufactured within the process window, relative to SiO_x/3JSC devices.

The microbeads have demonstrated their ability to lower the Fresnel reflection losses by providing a smooth optical transition from air to PDMS over a wide angular range. Therefore, they could be used to reduce reflection losses on various surfaces with refractive indices similar to PDMS, including SOEs used in CPV systems that inherently suffer from reflection losses on their air/glass interface. The application of a microbead coating would improve optical transmission and possibly improve the performance of the SOE or other optical elements.

ACKNOWLEDGEMENTS

We acknowledge the support from STACE, MITACS and Quebec Ministère de l'Économie, de la Science et de l'Innovation. LN2 is a joint International Research Laboratory (IRL 3463) funded and co-operated in Canada by Université de Sherbrooke (UdeS) and in France by CNRS as well as Université de Lyon (UdL, especially including ECL and INSA Lyon) and Université Grenoble Alpes (UGA). It is also supported by the Fonds de Recherche du Québec Nature et Technologie (FRQNT).

DATA AVAILABILITY STATEMENT

The data that support the findings of this study are available from the corresponding author upon reasonable request.

ORCID

Gavin P. Forcade https://orcid.org/0000-0001-9527-5661
Abdelatif Jaouad https://orcid.org/0000-0002-1466-7346
Christopher E. Valdivia https://orcid.org/0000-0002-6072-2959
Karin Hinzer https://orcid.org/0000-0002-2414-6288
Maxime Darnon https://orcid.org/0000-0002-6188-7157

REFERENCES

1. Aqachmar Z, Bouhal T, Lahrech K. Energetic, economic, and environmental (3 E) performances of high concentrated photovoltaic large scale installations: Focus on spatial analysis of Morocco. *Int J Hydrogen Energy*. 2020;45(18):10840-10861. https://doi.org/10.1016/j.ijhydene.2020.01.210
2. Oon LV, Tan MH, Wong CW, Chong KK. Optimization study of solar farm layout for concentrator photovoltaic system on azimuth-elevation sun-tracker. *Sol Energy*. 2020;204:726-737. https://doi.org/10.1016/j.solener.2020.05.032
3. Nishimura A, Hayashi Y, Tanaka K, et al. Life cycle assessment and evaluation of energy payback time on high-concentration photovoltaic power generation system. *Appl Energy*. 2010;87(9):2797-2807. https://doi.org/10.1016/j.apenergy.2009.08.011
4. Fthenakis VM, Kim HC. Life cycle assessment of high-concentration photovoltaic systems. *Prog Photovoltaics Res Appl*. 2013;21(3):379-388. https://doi.org/10.1002/pip.1186
5. Fraunhofer ISE: Photovoltaics Report, updated: 27 July 2021. https://www.ise.fraunhofer.de/content/dam/ise/de/documents/publications/studies/Photovoltaics-Report.pdf
6. Kost C, Shammugan S, Julch V, Nguyen H-T, Schlegl T. Levelized cost of electricity–renewable energy technologies. 2018.
7. Raut HK, Ganesh VA, Nair AS, Ramakrishna S. Anti-reflective coatings: a critical, in-depth review. *Energ Environ Sci*. 2011;4(10):3779-3804. https://doi.org/10.1039/c1ee01297e
8. Huang YF, Chattopadhyay S, Jen YJ, et al. Improved broadband and quasi-omnidirectional anti-reflection properties with biomimetic silicon nanostructures. *Nat Nanotechnol*. 2007;2(12):770-774. https://doi.org/10.1038/nnano.2007.389
9. Cannavale A, Fiorito F, Manca M, Tortorici G, Cingolani R, Gigli G. Multifunctional bioinspired sol-gel coatings for architectural glasses. *Build Environ*. 2010;45(5):1233-1243. https://doi.org/10.1016/j.buildenv.2009.11.010
10. Rambo CR, Cao J, Rusina O, Sieber H. Manufacturing of biomorphic (Si, Ti, Zr)-carbide ceramics by sol-gel processing. *Carbon N Y*. 2005;43(6):1174-1183. https://doi.org/10.1016/j.carbon.2004.12.009
11. Kennedy SR, Brett MJ. Porous broadband antireflection coating by glancing angle deposition. *Appl Optics*. 2003;42(22):4573-4579. https://doi.org/10.1364/ao.42.004573
12. Steele JJ, Brett MJ. Nanostructure engineering in porous columnar thin films: Recent advances. *J Mater Sci Mater Electron*. 2007;18(4):367-379. https://doi.org/10.1007/s10854-006-9049-8
13. Nam SH, Choi JW, Cho SJ, Kim KS, Boo JH. Growth of TiO 2 anti-reflection layer on textured Si (100) wafer substrate by metal-organic chemical vapor deposition method. *J Nanosci Nanotechnol*. 2011;11(8):7315-7318. https://doi.org/10.1166/jnn.2011.4813
14. Xi JQ, Schubert MF, Kim JK, et al. Optical thin-film materials with low refractive index for broadband elimination of Fresnel reflection. *Nat Photonics*. 2007;1(3):176-179. https://doi.org/10.1038/nphoton.2007.26
15. Xi J-Q, Kim JK, Schubert EF, et al. Very low-refractive-index optical thin films consisting of an array of SiO_2 nanorods. *Opt Lett*. 2006;31(5):601-603. https://doi.org/10.1364/ol.31.000601
16. Britten JA, Thomas IM. Sol-gel metal oxide and metal oxide/polymer multilayers applied by meniscus coating. In: Bennett HE, Chase LL, Guenther AH, Newnam BE, Soileau MJ, eds. *Laser-Induced Damage Optical Materials*. Vol.2114; 1993:244-250. https://doi.org/10.1117/12.180885
17. Nositschka WA, Beneking C, Voigt O, Kurz H. Texturisation of multicrystalline silicon wafers for solar cells by reactive ion etching through colloidal masks. *Sol Energy Mater sol Cells*. 2003;76(2):155-166. https://doi.org/10.1016/S0927-0248(02)00214-3
18. Yu P, Chiu M-Y, Chang C-H, et al. Towards high-efficiency multi-junction solar cells with biologically inspired nanosurfaces. *Prog*

Photovoltaics Res Appl. 2014;22(3):300-307. https://doi.org/10.1002/pip.2259

19. Chiu M-Y, Chang C-H, Tsai M-A, Chang F-Y, Yu P. Improved optical transmission and current matching of a triple-junction solar cell utilizing sub-wavelength structures. *Opt Express*. 2010;18(S3):A308-A313. https://doi.org/10.1364/oe.18.00a308
20. Asoh H, Oide A, Ono S. Formation of microstructured silicon surfaces by electrochemical etching using colloidal crystal as mask. *Electrochem Commun*. 2006;8(12):1817-1820. https://doi.org/10.1016/j.elecom.2006.08.021
21. Buencuerpo J, Torné L, Álvaro R, Llorens JM, Dotor ML, Ripalda JM. Nano-cones for broadband light coupling to high index substrates. *Sci Rep*. 2016;6(1):1-7. https://doi.org/10.1038/srep38682
22. Garciá-Linares P, Dominguez C, Dellea O, et al. Improving optical performance of concentrator cells by means of a deposited nanopattern layer. *AIP Conf. Proc.* 2015;1679(1):040004-1-040004-9. https://doi.org/10.1063/1.4931515
23. Delléa O, Shavdina O, Fugier P, Coronel P, Ollier E, Désage SF. Control methods in microspheres precision assembly for colloidal lithography. *IFIP Adv Inf Commun Technol*. 2014;435:107-117. https://doi.org/10.1007/978-3-662-45586-9_14
24. Forcade G, Valdivia CE, St-Pierre P, et al. Nanostructured surface for extended temperature operating range in concentrator photovoltaic modules. *AIP Conf. Proc.* 2020;2298:050002-1-050002-6. https://doi.org/10.1063/5.0032134
25. SYLGARD. 184 Silicone Elastomer 2017. https://www.dow.com/en-us/document-viewer.html?ramdomVar=1321611859083267856&docPath=/content/dam/dcc/documents/en-us/productdatasheet/11/11-31/11-3184-sylgard-184-elastomer.pdf
26. Schneider F, Draheim J, Kamberger R, Wallrabe U. Process and material properties of polydimethylsiloxane (PDMS) for optical MEMS. *Sensors Actuators, a Phys*. 2009;151(2):95-99. https://doi.org/10.1016/j.sna.2009.01.026
27. Miller DC, Kempe MD, Muller MT, Gray MH, Araki K, Kurtz SR. Durability of polymeric encapsulation materials in a PMMA/glass concentrator photovoltaic system. *Prog Photovoltaics Res Appl*. 2016;24(11):1385-1409. https://doi.org/10.1002/PIP.2796
28. Hasan O, Arif AFM. Performance and life prediction model for photovoltaic modules: Effect of encapsulant constitutive behavior. *Sol Energy Mater Sol Cells*. 2014;122:75-87. https://doi.org/10.1016/j.solmat.2013.11.016
29. Malitson IH. Interspecimen comparison of the refractive index of fused silica. *J Opt Soc Am*. 1965;55(10):1205-1209.
30. Delléa O, Lebaigue O. Boostream: a dynamic fluid flow process to assemble nanoparticles at liquid interface. *Mech Ind*. 2017;18(6):1-7. https://doi.org/10.1051/meca/2017026
31. Dellea O, Lebaigue O, Poncelet O. Method for forming a film of particles on the surface of a substrate. WO2020212286A1, 2020.
32. Wong EJ. *Modeling and control of rapid cure in polydimethylsiloxane (PDMS) for microfluidic device applications*. Massachusetts Institute of Technology; 2010.
33. Battaglia C, Hsu CM, Söderström K, et al. Light trapping in solar cells: can periodic beat random? *ACS Nano*. 2012;6(3):2790-2797. https://doi.org/10.1021/nn300287j
34. Siefer G, Baur C, Bett AW. External quantum efficiency measurements of Germanium bottom subcells: Measurement artifacts and correction procedures. *Conf. Rec. IEEE Photovolt. Spec. Conf*. 2010;704-707. https://doi.org/10.1109/PVSC.2010.5616919
35. Meusel M, Baur C, Létay G, Bett AW, Warta W, Fernandez E. Spectral response measurements of monolithic GaInP/Ga (In)As/Ge triple-junction solar cells: Measurement artifacts and their explanation. *Prog Photovoltaics Res Appl*. 2003;11(8):499-514. https://doi.org/10.1002/pip.514
36. Ferry VE, Verschuuren MA, van Lare MC, Schropp REI, Atwater HA, Polman A. Optimized spatial correlations for broadband light trapping nanopatterns in high efficiency ultrathin film a-Si:H solar cells. *Nano Lett*. 2011;11(10):4239-4245. https://doi.org/10.1021/nl202226r
37. Schäfer J, Foest R, Quade A, Ohl A, Weltmann KD. Local deposition of SiOx plasma polymer films by a miniaturized atmospheric pressure plasma jet (APPJ). *J Phys D Appl Phys*. 2008;41(19):194010. https://doi.org/10.1088/0022-3727/41/19/194010
38. Hugonin JP, Lalanne P. *Reticolo software for grating analysis*. arXiv preprint arXiv:2101.00901; 2021.
39. Byrnes SJ. *Multilayer optical calculations*. arXiv preprint arXiv:1603.02720; 2016.
40. Gupta V, Probst PT, Goßler FR, et al. Mechanotunable surface lattice resonances in the visible optical range by soft lithography templates and directed self-assembly. *ACS Appl Mater Interfaces*. 2019;11(31):28189-28196. https://doi.org/10.1021/acsami.9b08871
41. Kim Y, Lee SM, Park CS, Lee SI, Lee MY. Substrate dependence on the optical properties of Al2O3 films grown by atomic layer deposition. *Appl Phys Lett*. 1997;71(25):3604-3606. https://doi.org/10.1063/1.120454
42. Ochoa-Martínez E, Barrutia L, Ochoa M, et al. Refractive indexes and extinction coefficients of n- and p-type doped GaInP, AlInP and AlGaInP for multijunction solar cells. *Sol Energy Mater Sol Cells*. 2018;174:388-396. https://doi.org/10.1016/j.solmat.2017.09.028
43. Cui J, Allen T, Wan Y, et al. Titanium oxide: a re-emerging optical and passivating material for silicon solar cells. *Sol Energy Mater sol Cells*. 2016;158:115-121. https://doi.org/10.1016/j.solmat.2016.05.006
44. Djurišić AB, Rakić AD, Kwok PCK, Li EH, Majewski ML, Elazar JM. Modeling the optical constants of AlxGa1-xAs alloys. *J Appl Phys*. 1999;86(1):445-451. https://doi.org/10.1063/1.370750
45. Palik E. *Handbook of Optical Constants of Solids*. 3rd ed. Academic Press; 1998.
46. Aspnes DE, Studna AA. Dielectric functions and optical parameters of Si, Ge, GaP, GaAs, GaSb, InP, InAs, and InSb from 1.5 to 6.0 eV. *Phys Rev B*. 1983;27(2):985-1009. https://doi.org/10.1103/PhysRevB.27.985
47. Bedjaoui M, Despax B, Caumont M, Bonafos C. Si nanocrystal-containing SiO_x ($x < 2$) produced by thermal annealing of PECVD realized thin films. *Mater. Sci. Eng. B Solid-State Mater. Adv. Technol.* 2005;124–125:508-512. https://doi.org/10.1016/j.mseb.2005.08.066
48. Carneiro JO, Machado F, Rebouta L, et al. Compositional, optical and electrical characteristics of SiO_x thin films deposited by reactive pulsed DC magnetron sputtering. *Coatings*. 2019;9(8):1-18. https://doi.org/10.3390/coatings9080468
49. Zhang G, Cao Y, Zhang Y, Song X, Lu J, Li S. Preparation and characteristic analysis of ultra-low dielectric constant nano-porous silicon oxide films. *Lect. Notes Electr. Eng.* 2020;600:730-736. https://doi.org/10.1007/978-981-15-1864-5_99
50. Zhang Q, Xu JJ, Chen HY. Patterning microbeads inside poly (dimethylsiloxane) microfluidic channels and its application for immobilized microfluidic enzyme reactors. *Electrophoresis*. 2006;27(24):4943-4951. https://doi.org/10.1002/ELPS.200600024

How to cite this article: Forcade GP, Ritou A, St-Pierre P, et al. Microstructured antireflective encapsulant on concentrator solar cells. *Prog Photovolt Res Appl*. 2021;1-9. doi: 10.1002/pip.3468